Comparisons of CFD Simulations of Icing Wind Tunnel Clouds with Experiments Conducted at the NASA Propulsion Systems Laboratory

Tadas P. Bartkus[1]
Ohio Aerospace Institute, Cleveland, OH, 44142, USA

Peter M. Struk[2]
NASA Glenn Research Center, Cleveland, OH, 44135, USA

This paper evaluates simulation predictions against experimental test data of icing clouds that were produced during 2018 ice crystal icing physics tests conducted at the NASA Propulsion Systems Laboratory icing wind tunnel. Aero-thermal and cloud parameters are set and known upstream at the tunnel inlet and spray system, but change as the cloud and air thermodynamically interact as the flowing masses reach the tunnel test section. Utilizing the ANSYS Fluent Discrete Phase Model function, 3D computational fluid dynamics (CFD) simulations were performed, capturing the thermodynamic interactions between the test parameters, and providing predictions of the aero-thermal and cloud conditions at the tunnel test section. Simulation predictions were compared with test data that were measured at the tunnel exit plane. Evaluations focused on the cloud concentration (total water content), humidity content, and air temperature. CFD simulation predictions showed areas of agreement and disagreement. Simulations showed that cloud concentration profiles at the test section are strongly related to the initial spray nozzle pattern used at the tunnel inlet. Experimental data suggest that greater dispersion of the cloud occurred as the simulated cloud predicted areas of high and low cloud concentration compared to test data profiles. Simulations, however, captured the magnitude and location of the change in humidity content and the change in air temperature due to the presence of the cloud reasonably well, when compared to test data. This result would suggest that while the ANSYS simulation did not fully predict the spreading of the cloud as measured during experiment, it did capture evaporation and the molecular movements of air and vapor relatively well.

I. Nomenclature

A	=	area
m	=	mass (g or kg)
MMR	=	mass mixing ratio, defined as water vapor mass divided by the dry air mass (g kg^{-1} or kg kg^{-1})
MVD	=	median volumetric diameter (μm)
p	=	pressure (kPa or psi)
Q	=	Volumetric flow rate (m^3/s)
RH	=	relative humidity (%)
T	=	temperature (K or °C)

[1] Senior Research Associate, Icing Branch, 21000 Brookpark Road, MS 11-1, AIAA Senior Member
[2] Aerospace Engineer, Icing Branch, 21000 Brookpark Road, MS 11-2, AIAA Senior Member

TWC	=	total water content, defined as the sum of liquid water mass and ice water mass (g m^{-3} or kg m^{-3})
$TWC_{e,bulk}$	=	bulk total water content, as averaged over a given area at the tunnel exit (g m^{-3} or kg m^{-3})
U	=	air velocity (m s^{-1})
X	=	in the tunnel axial direction (m or in)
Y	=	in the tunnel vertical direction (m or in)
Z	=	in the tunnel lateral direction (m or in)
Δ	=	change

Subscripts

air	=	air
e	=	exit (or outlet)
i	=	inlet (or initial or injected)
water	=	water
0	=	total condition

II. Introduction

There have been numerous reports of turbofan engine power-loss or damage events that have been attributed to the ingestion of ice crystals [1]. These events typically occur in deep convective updraft systems and have included engine stall, rollback, flameout, surge, and engine component damage. Mason et al. [2] theorized that ice crystals ingested into the engine undergo partial melting within the warm compressor system and then, as a mixed-phase water mass, accrete on surfaces within the engine core. Research efforts in understanding the physics of ice crystal icing has grown to address this threat of engine icing. The National Aeronautics and Space Administration (NASA) Glenn Research Center has been conducting experiments to better understand ice crystal icing. Multiple engine tests have been conducted at the NASA Propulsion Systems Laboratory (PSL) icing wind tunnel since the tunnel's spray bar installation [3-5]. In addition, experimental studies on the fundamental physics of ice crystal icing have been conducted at the NASA PSL tunnel [6-9]. These icing tests and the work in this paper are part of NASA's Advanced Air Transport Technology (AATT) Project roadmap to improve understanding of the ice growth physics and improve engine aero-thermodynamic modeling tools to predictively assess the onset and growth of ice in current and future engines during flight.

The aim of the most recent fundamental ice crystal icing research effort in 2018 was to generate ice shapes on an airfoil model under well-characterized conditions [6, 7]. Ice shapes were generated across different flow conditions. As in previously conducted fundamental icing physics tests [8, 9], radial variations in the flow and cloud existed at the tunnel test section (exit plane), due to the selected nozzle pattern located upstream at the tunnel inlet. Previous experimental calibration efforts have been limited to centerline measurements [10-13]. To more accurately characterize the radial variations, an instrument traversing system was developed which allowed for the ability to perform flow surveys at various positions within the cloud at the tunnel exit plane.

Previous 3D computational fluid dynamics (CFD) simulations were run with a focus to better understand the flow and particle behavior leading up to the test section of PSL [14]. Simulations were performed utilizing the tunnel converging geometry, and included the tunnel spray bar system with supports. This study found that the particle pattern at the test section was influence by the upstream spray bar and support structure, and that vortex shedding aided in dispersing the particles. Furthermore, the crosswise vortex shedding at the spray bar converted into streamwise vortices as flow developed further downstream. The simulation work, however, did not include particle physics such as evaporation and phase change, as the particles were treated as rigid spheres.

During the 2018 icing tests, and on previous occasions [15-18], it has been observed that the conditions at the test section, most notably air temperature and humidity, change when the icing cloud is activated. A 1D thermodynamic model, TADICE, had been developed in-house and showed that a thermodynamic interaction between the icing cloud and flowing air accounts for the different aero-thermal conditions at the test section, compared with pre-spray conditions [19-23]. The TADICE model assumes uniformity at any cross-section along the tunnel axis (i.e. 1D), and therefore does not account for any radial variation that may exist. Radial variation in temperature and humidity, water content, cloud phase, and cloud particle size were measured during the 2018 tests. To address this non-uniformity, 3D CFD simulations were run using ANSYS Fluent to help better understand the complex thermodynamic interactions between the test parameters, and provide greater confidence of the aero-thermal and cloud conditions across the entire cross-section at the tunnel test section. Full 3D simulations were performed as the spray nozzle pattern selected to generate the cloud in the PSL tunnel was not radially or circumferentially symmetric. This paper describes the methodology to create the simulations and evaluates the simulation results with experimental data. Two complementary papers submitted for publication for this conference present detailed radial measurement analysis of air temperature and humidity [24], as well as total water content (*TWC*), melt ratio (liquid water mass divided by the total water mass), and particle size distribution [25].

III. Experiment Description

The NASA PSL is an altitude jet-engine test facility that generates ice particles and mixed-phase clouds using a liquid water spray nozzle system whereby the injected water droplets can freeze-out as the cloud propagates towards the test section [10-13]. The droplets freeze due to convective heat transfer and evaporative cooling. Figure 1 depicts the PSL geometry used for the fundamental icing physics tests. The PSL icing tunnel has an axial distance of 8.84 m (29.0 ft) from the plenum (tunnel inlet) to the test section (tunnel exit). The spray nozzles and spray bar system are located at the tunnel inlet in the plenum. The test section is a 0.91-m (36-in) diameter free-jet exit. City water (i.e. untreated water) was used for all experiments described in this paper. Icing occurred on a 0.267-m NACA0012 airfoil located 0.13 m beyond the tunnel exit in the free jet stream. The icing tests characterized the aero-thermal and cloud conditions utilizing a multi-instrument traversing system, where the instruments were able to probe the free jet at various positions of the cloud.

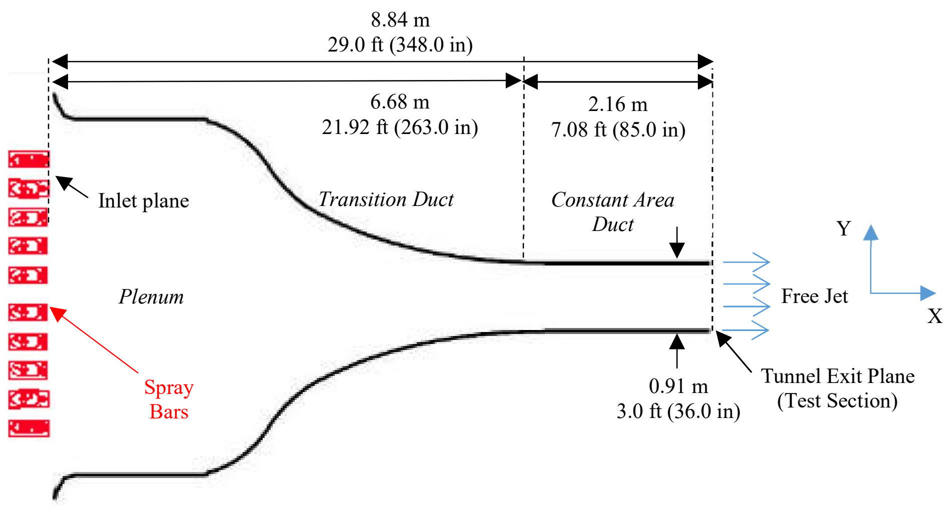

Figure 1: PSL tunnel geometry used for the fundamental ice-crystal icing physics tests with spray nozzles located at the tunnel inlet whereas the aero-thermal and cloud measuring instruments were located in the free jet in the test section.

A spray nozzle configuration was chosen that attempted to maintain the center circle area with a radius of 0.08 m (3 in) approximately uniform at the test section, and contain the entire cloud within a circle area with a radius of 0.30 m (12-in) radius. Figure 2 shows a diagram of the spray nozzle system configuration with the two spray nozzle patterns that were primarily used for these tests. The red and blue ellipses of Fig. 2 represent the approximate initial area coverage for the two different spray patterns. Figures 1 and 2 show the Cartesian coordinate system (X, Y, and Z) used, where the coordinates origin (0, 0, 0) exists at the center of the inlet plane.

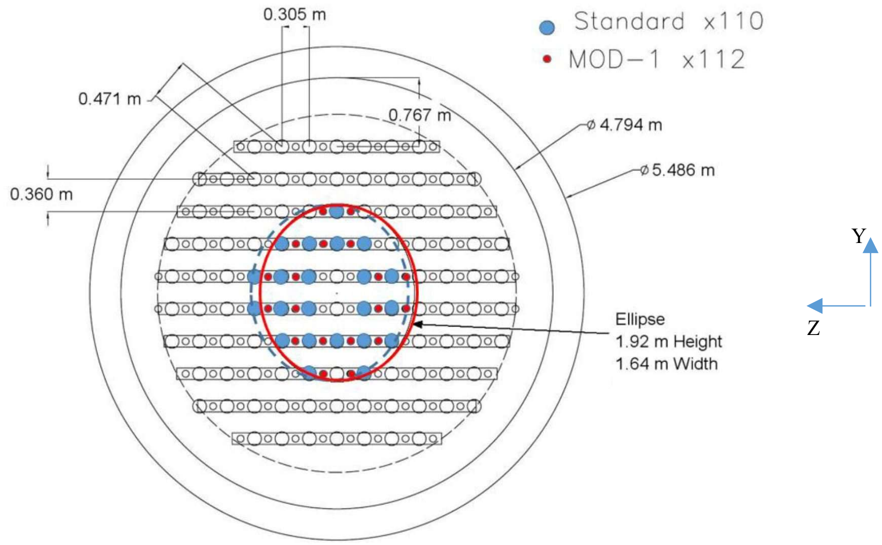

Figure 2: The PSL spray bar geometry and the two nozzle patterns used during testing. The filled-in red circles denote the pattern for the Mod-1 nozzles (19 total) whereas the blue filled-in circles denote the pattern for the Standard nozzles (22 total). The ellipses, colored to match the nozzle type, denote the approximate initial coverage area of the spray. The view is aft-looking-forward.

The primary objective for the tests was to generate ice shapes on the NACA0012 airfoil across multiple well-characterized conditions [6, 7]. Table 1 provides the target conditions for 5 main test conditions that were run. Radial variation of aero-thermal and cloud conditions at the test section were measured with various instruments for four test conditions (Test Conditions # I, II, III, and V), and will be the focus of this paper. Test condition numbering was chosen to match convention from previous papers [6, 7]. The tunnel exit velocity, U_e, total pressure, p_0, total temperature, T_0, total relative humidity, RH_0, and bulk total water content at the tunnel exit, $TWC_{e,bulk}$, are shown in Table 1. RH_0 values are provided in the table for the 4 test conditions that were radially probed, whereas no value is provided for Test Condition # IV (not evaluated in this paper). With respect to the radial traverse test conditions, tests were conducted at three target velocities (85 m/s, 135 m/s, and 185 m/s), and at two bulk total water contents (about 2 and 5 g/m^3). The target air flow speeds equate to Mach values of 0.25, 0.40, and 0.56 respectively. In addition, the injected particle size distribution was held constant for each test with an approximate initial median volumetric diameter, MVD_i, of 20 µm. The overall aim for the tests was to generate a mixed phase cloud, as would exist within a warm engine, and produce ice accretions on a model airfoil. The conditions listed in Table 1 generated the desired mixed phase cloud, where the resulting wet-bulb temperatures were slightly below 0 ^{O}C to promote partial freezing of the liquid cloud. Wet-bulb temperature is the surface temperature of an evaporating volatile substance, in this case the temperature that the water particles in the cloud tend to reach.

Table 1: List of target conditions for 5 main test which were run. Radial characterization of the air and cloud at the tunnel exit was performed for Test Conditions # I, II, III and V.

Test Condition #	U_e m/s	p_0 kPa (psia)	T_0 ºC	RH_0 %	$TWC_{e,bulk}$ g/m^3
I	85	44.8 (6.5)	7.2	34	2.2
II	135	44.8 (6.5)	7.2	33	2.0
III	185	44.8 (6.5)	7.2	33	2.1
IV	135	87.6 (12.7)	7.2	N/A	2.0
V	135	44.8 (6.5)	7.2	35	5.0

It should be noted that the $TWC_{e,bulk}$ values in Table 1 represent the bulk content of water averaged over 0.30 m (12 in) of the 0.46-m (18-in) tunnel exit radius, with no loss due to evaporation or sublimation. Equation (1) shows that $TWC_{e,bulk}$ is the ratio of water mass flow rate, $\dot{m}_{water}$, to volumetric flow rate of air, Q_{air}. A step further, Q_{air} is the product of the exit velocity and area, A, where A in this case was chosen to equal the area of the circle with a radius

0.30 m. For these experiments, the nozzle configuration was selected to contain the cloud within this 0.30 m radius. It can be seen that the value chosen for A can vary the resulting $TWC_{e,bulk}$, and must be explicitly defined.

$$TWC_{e,bulk} = \frac{\dot{m}_{water}}{Q_{air}} = \frac{\dot{m}_{water}}{U_e A} \tag{1}$$

Several instruments were utilized to characterize the aero-thermal and cloud conditions at the tunnel exit for the fundamental icing physics tests. The liquid and ice water content of the cloud was measured using the Science Engineering Associates Multiwire probe (MW) [26], and the Ice Crystal Detector (ICD) [27]. The total water content was measured using the Science Engineering Associates Isokinetic Probe, version 2 (IKP) [28]. The MW measurements presented in this paper are not corrected for collision efficiency [25]. Particle size measurements were made using Artium Technologies' High Speed Imaging (HSI) and Phase-Doppler Interferometer (PDI) probes [29]. Humidity content and total air temperature was measured by a Rearward-Facing Probe (RFP) that was developed in-house [22-24]. In addition, the Rosemount forward-facing Total Air Temperature (TAT) probe was also used to measure air temperature [30]. Finally, cloud uniformity was assessed using a tomography system [31] that generated a two dimensional (2D), time-averaged, intensity map of the cloud across a portion of the 0.46-m (18-in) radius duct. A detailed description of the experimental configuration, the data collected, and results of the fundamental ice crystal icing physics tests can be found elsewhere [6, 7].

Radial characterization of the air and cloud at the tunnel exit were done at discrete points utilizing the multi-instrument traversing system. Figure 3 shows the locations that were probed in Cartesian coordinates (Z-Y axes). The Cartesian coordinate system is labeled accordingly with the simulation coordinate system. A numbering system (0-15) was utilized for easy reference during testing, with location 0 as the centerline. In Fig. 3, bold coordinates are listed in meters, whereas the coordinates listed in parenthesis are in inches.

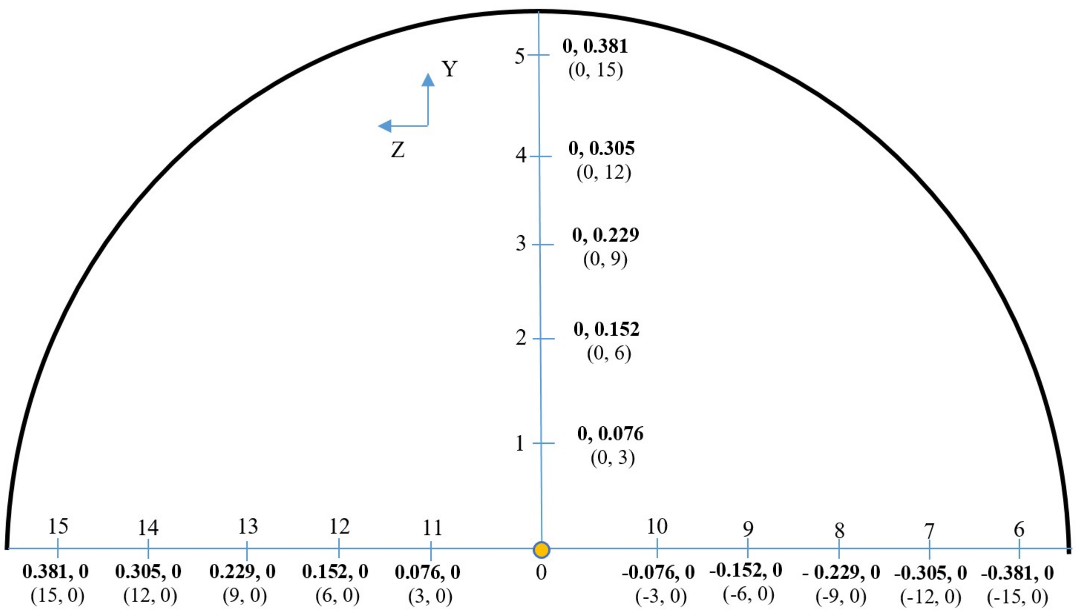

Figure 3: Instrument probing locations and numbering at the tunnel exit. The schematic is viewed aft-looking-forward. The Cartesian coordinate system is shown in meters (bold) and inches (parentheses) and is labeled accordingly with the simulation coordinate system (i.e. companion papers may have Z-axis coordinate reversed).

IV. Simulation Descriptions

The following section outlines the general methodology that was used to run the CFD simulations of cloud development at PSL. In addition, this section provides a brief description of the 1D TADICE model whose simulation predictions are also compared with 3D CFD predictions and experimental measurements, as a reference.

A. 3D CFD Simulation Geometry and Mesh Generation with Pointwise

The geometry and discrete point meshing of the PSL tunnel was created in Pointwise. The PSL tunnel was modeled from the exit plane of the spray nozzles (inlet) to the exit of the tunnel at the test section (outlet), where the 3D rendering can be seen in Fig. 4a. The volume of this 3D domain was discretized into 2.97 million points, which generated 2.96 million structured hexagon cells. Using the Pointwise Spacing Constraints function, finer grid spacing was applied near the tunnel wall boundaries to capture boundary layer effects. A surface layer cell height of about $Y^+=1$ was targeted, where Y^+ is a non-dimensional boundary layer quantity that is considered resolved with values equal to or below 1. Figure 4b shows a close-up view of the grid on the tunnel surface and tunnel exit plane.

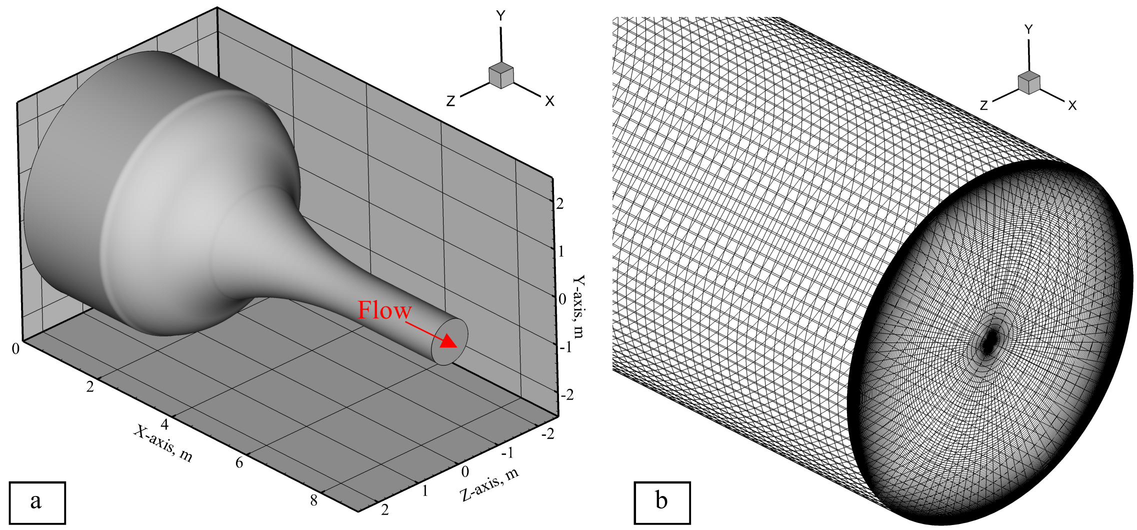

Figure 4: Images of the a) rendered 3D tunnel geometry and b) the grid as shown on the tunnel wall and at the tunnel exit plane.

B. 3D CFD Simulation Physics with ANSYS Fluent

Steady state CFD simulations were performed using ANSYS Fluent. The Discrete Phase Model (DPM) function was utilized to simulate the cloud particles. The DPM treats the fluid phase as a continuum by solving the Navier-Stokes Equations (Eulerian model), whereas the particles are tracked (Lagrangian model) through the calculated flow field. The discrete random walk model was used to mimic the effect of instantaneous turbulent velocity fluctuations on the particle trajectories. Two-way coupling of energy and mass exchange (i.e. convective heat transfer, and evaporation) was enabled to capture the thermodynamic interaction between the air and cloud. The Standard k-epsilon viscous model was utilized, with no slip boundary conditions at the tunnel wall. A 10% turbulence intensity at the inlet boundary was chosen for these simulations to account for the greater turbulence that the spray bar system generates in the flow, but which is not physically modeled. It should be noted, however, that the increased turbulence at the inlet likely does not capture the mixing that occurs downstream from large scale vortices which develop from flow over the spray bar system as simulated by Feier [14]. The DPM function allows for multiple ways of simulating the cloud particles. The cloud was simulated with individual spray nozzles (19 or 22 nozzles depending on the test condition) located at the tunnel inlet, as depicted in Fig. 2. A Rosin-Rammler distribution function was utilized to approximate the initial particle size distribution ejected out of the spray nozzles. The Lagrangian model tracks particles by grouping them into statistical parcels to reduce the computational workload of tracking individual particles. To reduce computational time, residual convergence criteria for all conservation equations were set to $1E^{-3}$, except for the continuity equation where the residual was set to $1E^{-2}$. Table A1 in the appendix provides details of several key parameters that were used as inputs for running the ANSYS Fluent simulation.

It should be noted that the DPM function allows for liquid to vapor phase change (evaporation), but does not have the ability to change phase from liquid to solid (freezing). A user defined function (UDF) must be written an implemented in order to simulate droplet freezing. Hence, if water droplets decrease below freezing temperatures, the particles act like supercooled droplets. In addition, the DPM function does not provide the ability to condense from vapor phase to liquid. When local relative humidity exceeds 100% (when saturation is exceeded), the DPM function treats the particles as inert (no condensation).

C. 1D TADICE Software Description

Simulations were run utilizing the in-house 1D TADICE software to predict aero-thermal and cloud conditions at the tunnel test section. Given initial aero-thermal (air temperature, humidity, pressure, and velocity) and cloud conditions (particle size distribution, water content, and water state), along with tunnel geometry, the model will solve conservation and compressible flow equations, and predict conditions at the tunnel exit plane. The mass and energy conservation equations between air and cloud are fully coupled. TADICE has the capability to model all phase changes, including freezing and condensation, whereas the ANSYS Fluent DPM function does not. TADICE, however, is a 1D model, and efforts were made to account for the non-uniform initial conditions. Since the nozzles selected for water injection into the tunnel were not uniform across the inlet, the model simulated only the inner core of the tunnel, assuming no exchange between the inner cloud core and the empty annulus. The inner core represents the blue and red ellipses in Fig. 2, and follows those streamlines axially to the tunnel exit plane. Therefore, TADICE predictions best represent conditions near the centerline of the tunnel. Total water content was calculated using the injected water mass for the given inner core area. $TWC_{e,bulk}$ values for the inner core equated to approximate 7 g/m^3 for Test Conditions # I, II and III, and was about 16 g/m^3 for Test Condition # V. Details of the TADICE model development can be found elsewhere [19, 20].

V. Simulation Results and Comparisons with Experimental Data

The ANSYS Fluent CFD simulation predictions, along with comparisons with experimental data, are presented in this section. The first sub-section provides key simulation predictions for a single condition that is representative of all conditions. The second sub-section compares simulation total water content, humidity, and temperature predictions with experimentally measured data at the tunnel exit plane. Finally, the third sub-section will compare total water content predictions with tomography measurements.

A. Representative 3D CFD Simulation Predictions

Key simulation predictions are presented here for Test Condition # II (U_e = 135 m/s and $TWC_{e,bulk}$ = 2.0 g/m^3), as they are qualitatively representative for the four test conditions. The predictions highlight the radial variation as well as the changes in conditions due to the cloud and air masses thermodynamically interacting.

Figures 5a and 5b show the simulation *TWC* cross-sectional contours of the tunnel center axis vertical plane and tunnel exit plane, respectively. For this test condition, 22 nozzles were activated (blue circles in Fig. 2). Figure 5 shows that *TWC* radial and circumferential variations exist down the axis of the tunnel and at the tunnel exit in large part due to the centralized spray nozzle configuration at the tunnel inlet. The spray nozzles selected created a core cloud-filled section and a cloudless annulus area. The cloud covers approximately the center 0.2 m radius at the tunnel exit plane. It should be noted that Fig. 5a shows the tunnel center axis vertical plane which happens to be where the two center spray nozzles in the vertical plane were not activated, which ultimately created the small centerline cloud vacancy. As a reminder, the target $TWC_{e,bulk}$ = 2.0 g/m^3 is the value averaged over the center 0.30-m radius at the exit plane, but local *TWC* high and low spots can exist. It can be seen in Fig. 5b that while some dispersion of the cloud occurred, higher concentrations of *TWC* generally exist along the nozzle streamlines. Local values reach as high as *TWC* = 8 g/m^3 at the tunnel exit plane. The contour range for Fig. 5a and 5b were kept the same, which resulted in clipped *TWC* values in Fig. 5a. Local *TWC* values in the tunnel plenum are greater than 8 g/m^3, as there is little dispersal of the cloud in the early stage of the cloud development. Note that the Fig. 5 presents *TWC* in kg/m^3.

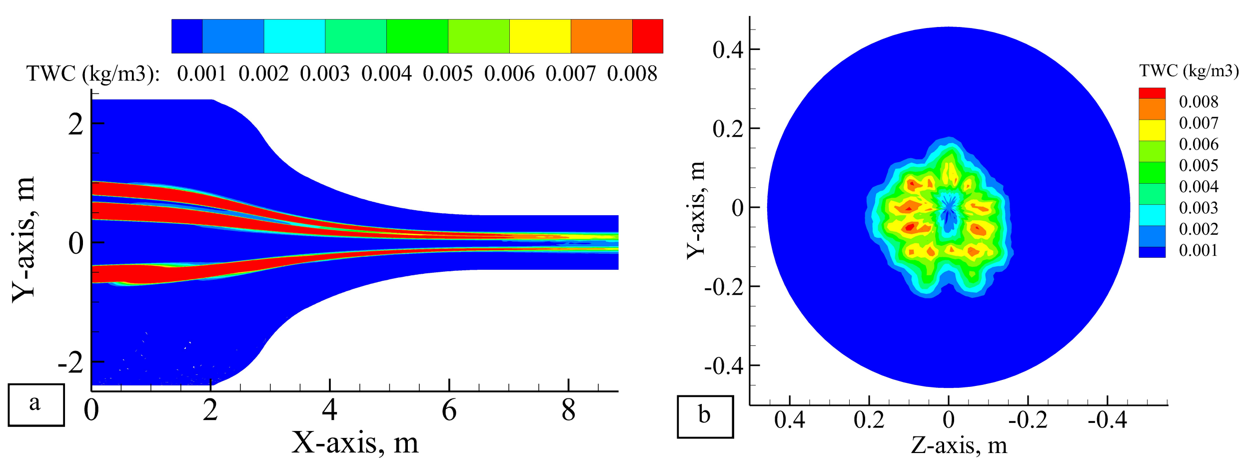

Figure 5: CFD simulation results showing the cross-section contours of the total water content a) along the center axis vertical plane, and b) at the tunnel exit plane. The Z-axis in Fig. 5b follows the sign convention from the aft-looking-forward perspective at the tunnel exit plane.

Figures 6a and 6b show the simulation predictions of mass mixing ratio, *MMR,* and total air temperature cross-sectional contours at the tunnel exit plane, respectively. The mass mixing ratio is defined as the ratio of water vapor mass to dry air mass. Since the flowing air is unsaturated at 33% RH_0 (i.e. sub-100% *RH*), there exists the potential to partially evaporate the injected liquid cloud. Due to the partial evaporation of the cloud, the water vapor mass content is greater in the central region at the tunnel exit plane. The evaporating cloud also reduces total air temperature. As portions of the water droplet cloud evaporate and get "promoted" from a lower liquid water energy level to at higher water vapor energy level, energy is removed from the surrounding air, resulting in a decreased air temperature at the tunnel exit plane. For the same reasons provided earlier in describing the *TWC* simulations, radial variations in *MMR* and T_0 exist at the tunnel exit due to the centralized spray nozzle configuration at the tunnel inlet. A RH_0 = 33% at the tunnel inlet equates to *MMR* = 0.0047 kg/kg, which remains constant in the outer annulus regions of the tunnel (blue contour in Fig. 6a) due to the centralized cloud. The change in mass mixing ratio, ΔMMR, due to cloud evaporation is about ΔMMR = 0.0027 kg/kg (~0.0075 minus 0.0047 kg/kg) in certain locations at the tunnel exit plane. Similarly, the tunnel inlet total air temperature of T_0 = 7.2 ^{O}C (280.3 K) remains constant in the outer annulus region (red contour in Fig. 6b) and the change in total air temperature, ΔT_0, due to cloud evaporation is about ΔT_0 = -7 K (~273 K minus 280 K) in certain locations at the tunnel exit plane. The value for ΔMMR and ΔT_0 is simply the change due to the presence of the cloud (cloud on minus cloud off). Of note, comparing the exit plane contours between *TWC* (Fig. 5b) and *MMR,* T_0 (Fig. 6), it can be seen that the *MMR* and T_0 are more diffuse than *TWC*. This suggests that the relatively large cloud droplets act in a more ballistic fashion, while the miniscule air and vapor molecules are subject to the random turbulence fluctuations.

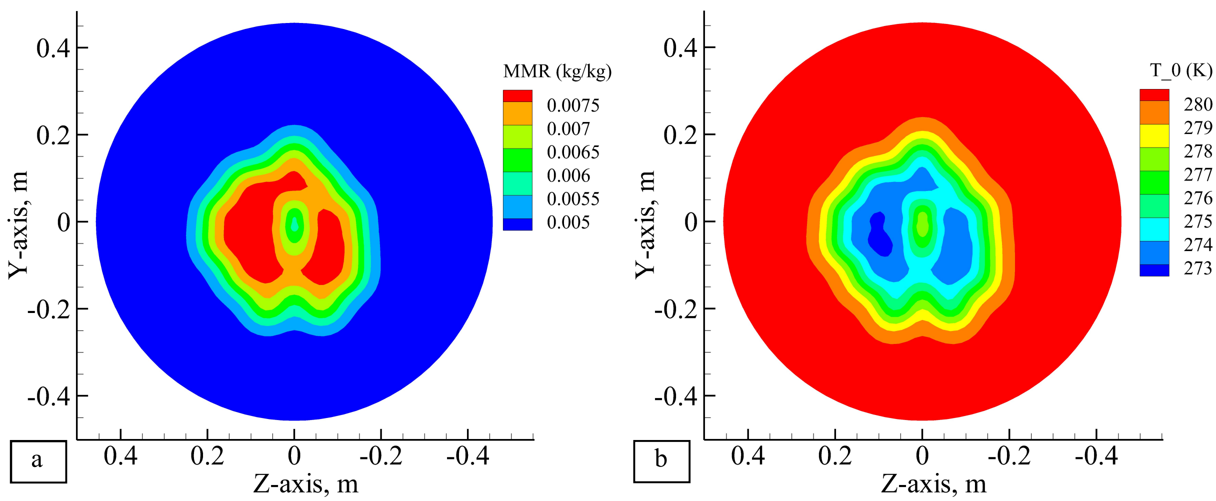

Figure 6: CFD simulation results showing the cross-section contours of the a) mass mixing ratio and, b) the total air temperature at the tunnel exit plane. The Z-axis in both contour plots follow the sign convention from the aft-looking-forward perspective at the tunnel exit plane.

B. Comparison Between Simulation and Experimental Temperature, Humidity and Total Water Content Data

CFD simulation results are compared with experimentally measured data in this sub-section. Comparisons of the four radial traverse test conditions (Test Conditions # I, II, III, and V) are presented here. Experimental data collected along the Y-axis (locations numbers 0-5 in Fig. 3) for Test Conditions # I, II, and III, and data from the Z-axis (locations 0, 10, 9, 8 in Fig. 3) for Test Condition # V, are compared with CFD simulation results. Total water content, ΔMMR, and ΔT_0 are compared. Table 2 lists the instrument and corresponding measurement that is used for comparison against simulation for Figs. 7-10 in this sub-section. Some instruments are able to provide two types of measurements when the cloud is activated. The Rosemount Total Air Temperature probe and Rearward Facing Probe (NASA in-house instrument) provide total air temperature measurements. The Rearward Facing Probe and Isokinetic Probe provide the humidity measurements. Finally, the Isokinetic Probe and Multiwire probe provide total water content measurements. The abbreviation used in Figs. 7-10 is provided in parenthesis in Table 2.

Table 2: List of instruments and corresponding measurements used for comparison with simulation for Figs. 7-10.

Instrument (Abbreviation used in Figs. 7-10)	Measurement
Multiwire probe (Exp - MW)	Total Water Content
Isokinetic Probe, version 2 (Exp - IKP)	Total Water Content
Isokinetic Probe, version 2 (Exp - IKP)	Humidity
Rearward Facing Probe (Exp - RFP)	Humidity
Rearward Facing Probe (Exp - RFP)	Total Air Temperature
Rosemount Total Air Temperature Probe (Exp - TAT)	Total Air Temperature

Figure 7 shows Test Condition # I (U_e = 85 m/s and $TWC_{e,bulk}$ = 2.2 g/m^3) comparisons of a) *TWC*, b) *ΔMMR*, and c) ΔT_0. The 3D ANSYS CFD simulation (Sim - ANS) as well as the 1D TADICE simulation prediction (Sim - TAD) are provided. The TADICE simulation is radially flat for all figures because it is a 1D model. The figures show the radial variation at the tunnel exit plane, which has a radius of about 0.46 m.

Figure 7a shows radial variation for both the 3D ANSYS simulation and experiment, however the location and magnitude of peak *TWC* values vary between simulation and experiment. The simulation *TWC* largely corresponds to the nozzle configuration at the tunnel inlet. As can be seen in Fig. 2, the nozzles that were used created a "donut-shape", where no nozzles were used at the very center (red circles, 19 nozzles). This pattern can be seen in Fig 7a, as there is low cloud density at the center (0 m), the highest cloud density where the nozzle streamlines would end at the exit plane, and then a rapid drop off in density moving out further radially. Experimentally, the maximum density occurs at the center, and decreases radially. The simulation does not predict as much dispersion of the cloud as measured experimentally, which would explain the disagreement in profile shape and magnitude. In both ANSYS simulation and experiment, no cloud exists in the outer annulus region at the tunnel exit plane. TADICE also over-predicts cloud density.

Figure 7b and 7c show that there is better agreement in the *ΔMMR* and ΔT_0 comparisons, respectively. There again exists a different location for maximum *ΔMMR* and ΔT_0 between experiment and ANSYS simulation as explained for *TWC*. However the maximum *ΔMMR* and ΔT_0 as predicted by simulation (ANSYS and TADICE) is similar to what was measured experimentally. This would suggest that the ANSYS simulation did not predict the spreading of the cloud as measured during experiment, but captured evaporation and the molecular movements of air and vapor relatively well. Of note is that total air temperature was measured to decrease by 6 K at the centerline when the cloud was activated. This is not an insignificant amount when accuracy in conditions at the test section is of importance. Just a single degree variance can be the difference between freezing and melting.

It should be noted that some experimental measurements provide repeat points at the centerline position (0 m). Figure 7b and 7c shows the variation in measurements that can occur with the same instrument for humidity and temperature, respectively.

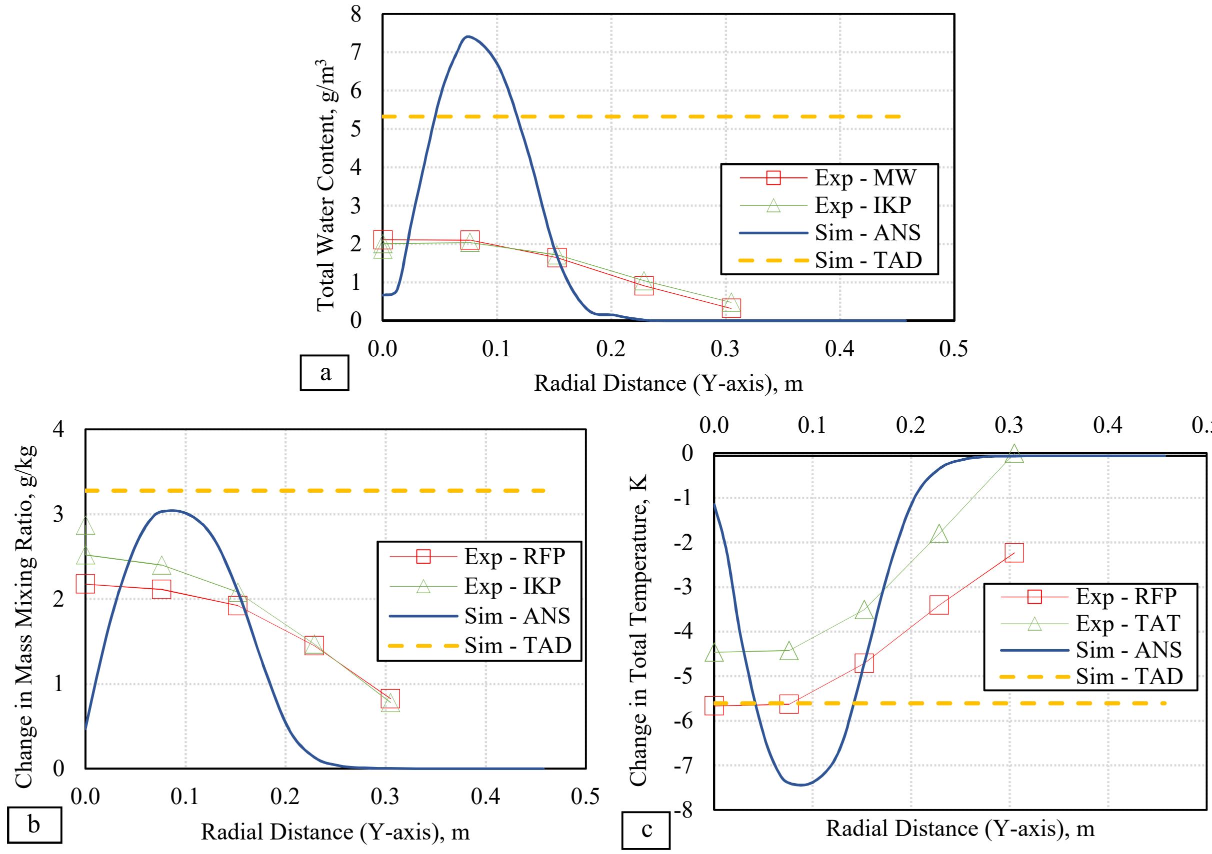

Figure 7: Test Condition # I comparison between simulation predictions and experimental data in the radial vertical direction (Y-axis) at the tunnel exit plane for a) total water content, b) change in mass mixing ratio, and c) change in total air temperature.

Figure 8 shows Test Condition # II (U_e = 135 m/s and $TWC_{e,bulk}$ = 2.0 g/m^3) comparisons. This is a higher velocity case, and uses the 22-nozzle configuration (blue circles in Fig.2). The *TWC* prediction in Fig. 8a has a similar profile shape as described for Test Condition I, but the magnitude matches more closely to experiment. It is hypothesized that the cloud concentrates more towards the centerline of the tunnel at higher velocities, which would explain the higher *TWC* measured in this higher velocity case, and why there is better agreement between simulation and experiment compared to Test Condition # I.

There is fair agreement of ΔMMR and ΔT_0 between experiment and ANSYS simulation as seen in Fig. 8b and 8c, respectively. Again, greater cloud dispersion could perhaps have resulted in even better agreement with experiment. TADICE predicted relatively well, when only comparing the centerline measurements.

It should be noted that the centerline measurement with the RFP became contaminated, and hence no temperature or humidity data are provided at 0 m for this instrument. In addition, the Rosemount TAT probe was not radially traversed for this test condition.

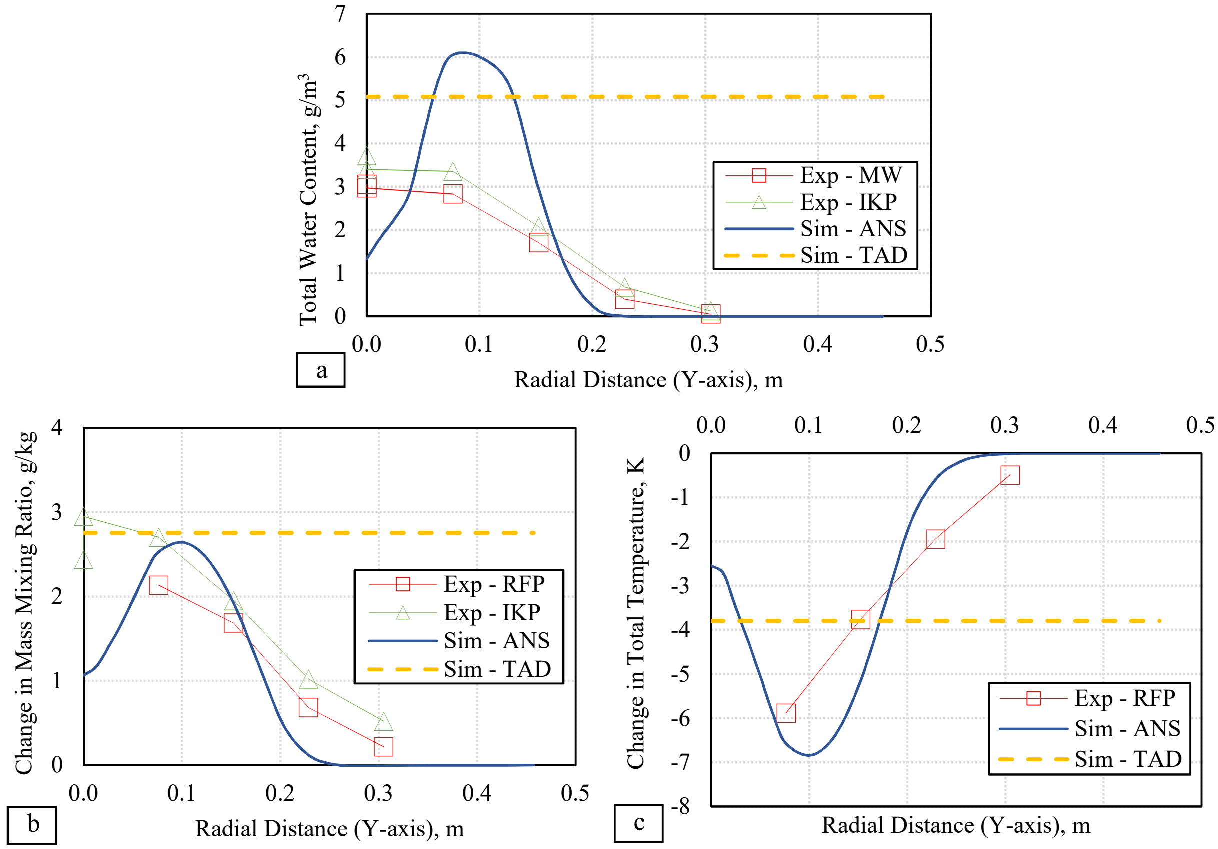

Figure 8: Test Condition # II comparison between simulation predictions and experimental data in the radial vertical direction (Y-axis) at the tunnel exit plane for a) total water content, b) change in mass mixing ratio, and c) change in total air temperature.

Figure 9 shows Test Condition # III (U_e = 185 m/s and $TWC_{e,bulk}$ = 2.1 g/m^3) comparisons. This was the highest velocity case, and also used the 22-nozzle configuration (blue circles in Fig.2). The *TWC* prediction in Fig. 9a has a similar profile shape as in the previous two test conditions. The higher 185 m/s air velocity case has resulted in an increased peak *TWC* measurement (IKP) compared to the slower velocity case of 135 m/s, supporting the centerline concentration hypothesis posed earlier. Both simulations captured this *TWC* increase, but still over-predicted peak *TWC,* as dispersion of the cloud is not sufficiently predicted. Some separation between the IKP and MW can be seen in Fig. 9a as the IKP historically tends to measure higher values than the MW probe due to lower ice collection and retention efficiency of the latter [28].

It should be noted that the RFP and Rosemount TAT probes were not radially traversed for this test condition, therefore there are no experimental temperature data and only humidity data from the IKP are provided. There is fair agreement of ΔMMR between experiment and ANSYS simulation as seen in Fig. 9b Temperature predictions are provided for completeness even though temperature data were not collected. TADICE has predicted smaller decreases in ΔT_0 and smaller increases of ΔMMR for increased velocity conditions compared to slower TADICE predictions. The main factor at play is that residence time decreases with higher velocity, which has resulted in less evaporation. This effect cannot be seen or determined clearly for the ANSYS simulations.

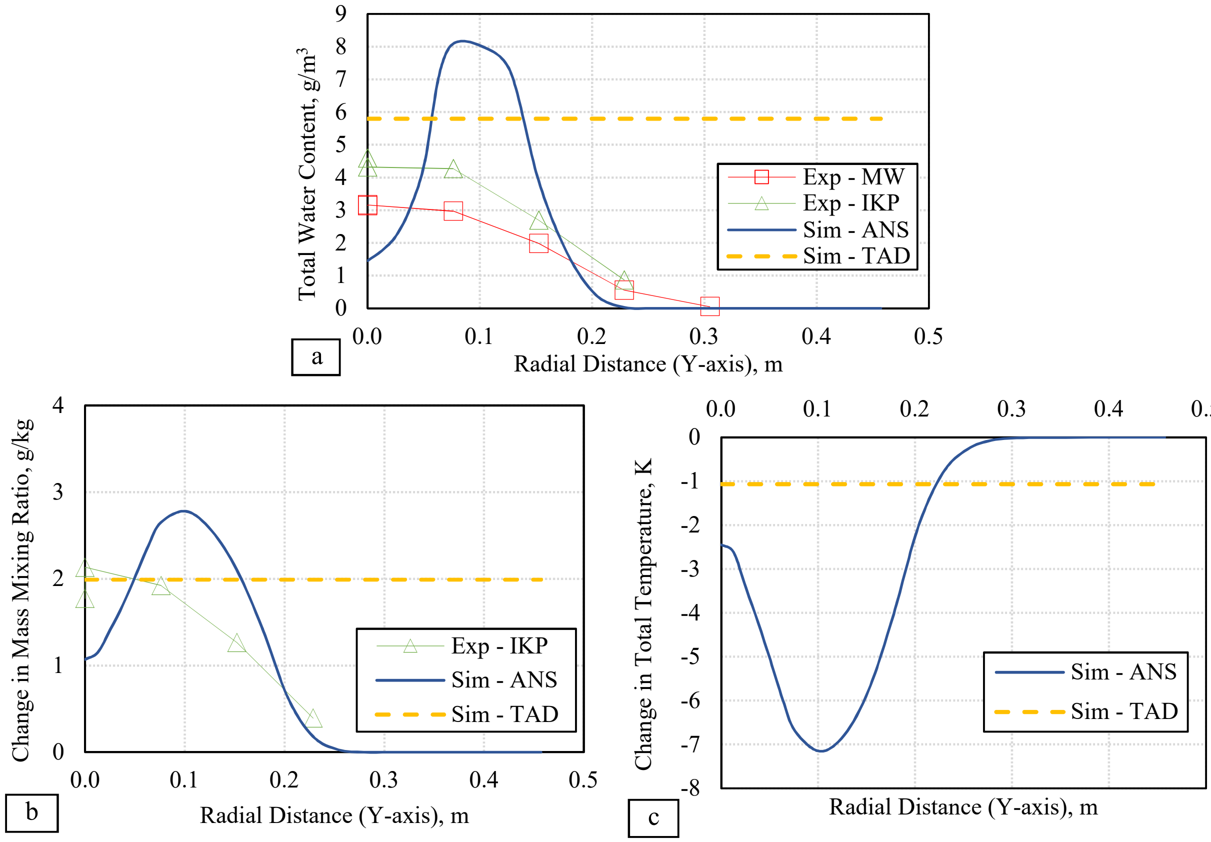

Figure 9: Test Condition # III comparison between simulation predictions and experimental data in the radial vertical direction (Y-axis) at the tunnel exit plane for a) total water content, b) change in mass mixing ratio, and c) change in total air temperature. Note, experimental temperature data were not collected for this test condition.

Figure 10 shows Test Condition # V (U_e = 135 m/s and $TWC_{e,bulk}$ = 5.0 g/m^3) comparisons. This was the high water loading case, and also used the 22-nozzle configuration (blue circles in Fig.2). The ANSYS simulation *TWC* profile in Fig. 10a is qualitatively similar to previous cases. The peak *TWC* values are greater for both experiment and simulation, due to the initial greater water loading, however the simulations over-predicts *TWC* by a fair amount. The ANSYS simulation under-scattering of the cloud again appears to be the cause for the difference between experiment and simulation.

The effects of cloud under-scattering cascades down to the ΔMMR and ΔT_0 predictions as well. There is greater deviation between ANSYS simulation and experiment as seen in Fig. 10b and 10c in this case, in particular the ΔT_0. TADICE predicts a small ΔT_0 as the high water loading provides heat to the air as the cloud partially freezes (latent heat release), nearly balancing the evaporative cooling effect on air temperature in this case. The current ANSYS simulation does not model freezing, and therefore does not capture the latent heat release as the cloud begins to freeze. In addition to properly predicting the cloud phase, implementing a user-defined function in ANSYS to simulate freezing will provide different air temperature predictions as well.

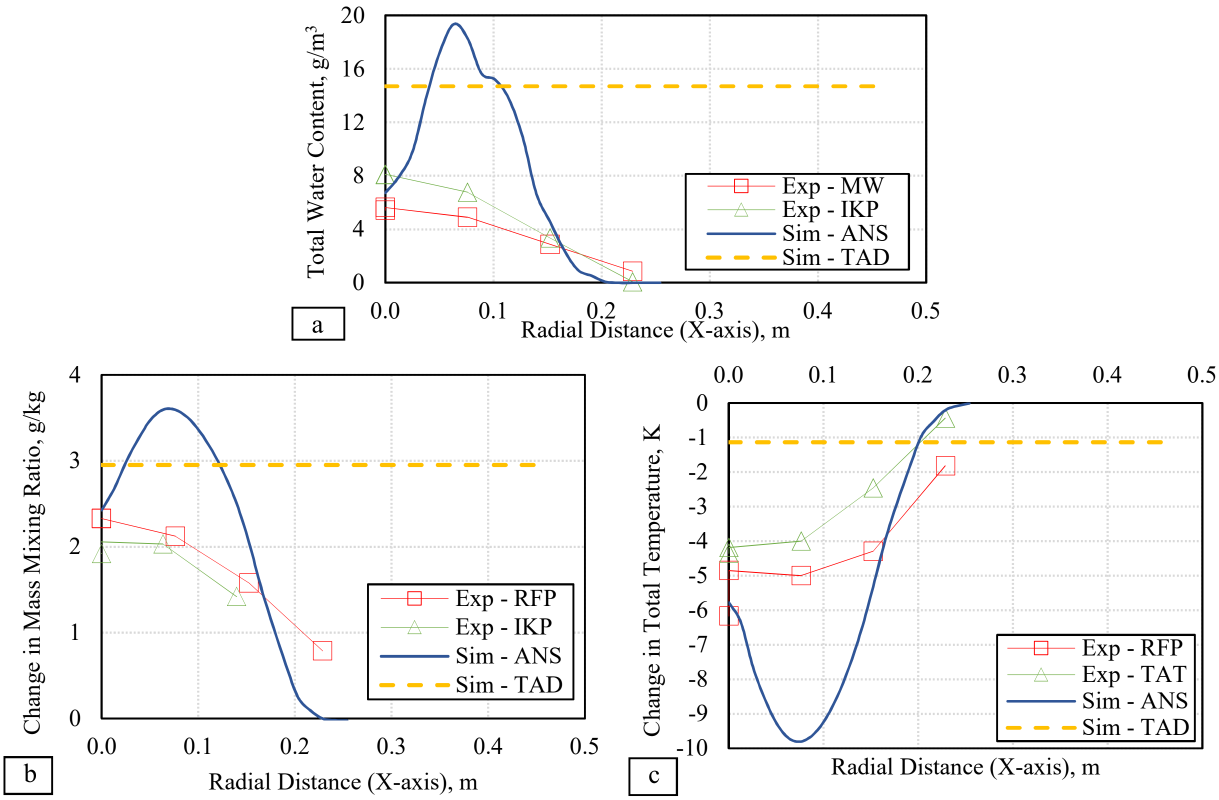

Figure 10: Test Condition # V comparison between simulation predictions and experimental data in the radial horizontal direction (X-axis) at the tunnel exit plane for a) total water content, b) change in mass mixing ratio, and c) change in total air temperature.

C. Comparison Between Simulation and Tomography Measurements

Tomography measurements were collected near the tunnel exit plane during IKP traverse tests. Figure 11 shows *TWC* comparisons between simulation predictions and tomography data for the four radial traverse test conditions. Simulation predictions at the tunnel exit plane are shown on the left (a, c, e, and g) whereas the corresponding tomography measurements are shown on the right (b, d, f, and h). Tomography, which shows a time averaged cloud concertation was scaled according to the centerline *TWC* as measured by the IKP. The Tomography is able to capture cloud concentrations for the inner 0.38 m of the 0.46 m radius tunnel. This tomography limit is indicated in each image in Figure 11. The circular physical size of the tomography measuring area is matched between simulation and experiment for easier comparison. In addition, the same numerical scale is used between the two for each test condition (0.0 - 0.008 kg/m^3 for Fig. 11a-f, and 0.0 - 0.024 kg/m^3 for Fig. 11g-h). Some high *TWC* concentrations were clipped at 0.008 kg/m^3 in Fig. 11e to maintain the same numerical scale for comparison purposes. Attempts were made to match the color scale. It should be noted that blue contour color in the simulation predictions is void of any cloud (*TWC* = 0 g/m^3), whereas the white and purple contour colors in the tomography images are effectively cloudless as well. These contour images allow for a more comprehensive perspective of cloud water content as compared to a single cross-sectional profile as in the previous sub-section.

Comparing simulation with tomography, it can be seen that a slightly more diffuse cloud was measured experimentally. This scatter applies both radially outward and inward as there was no low density hole measured in the center like there is with simulation. Along with the IKP and MW measurements, this is a third instrument indicating more mixing than simulation. As mentioned previously, this simulation under-scattering leads to the local high *TWC* concentrations. Looking at Test Conditions # I and V, the tomography suggests a much more scattered cloud occurred than what simulation predicted, and would explain why there is overall not good agreement. However, looking more closely at Test Conditions # II and III, and looking beyond the local high *TWC* concentrations, there is reasonable agreement for the bulk of the cloud areas, as represented in green contour colors for both simulation and experiment. Also, for the three consecutively increasing velocity cases (Test Conditions # I through III), increases in *TWC* can be seen both in simulation and experiment. This suggests that simulation is capturing some concentration aspects.

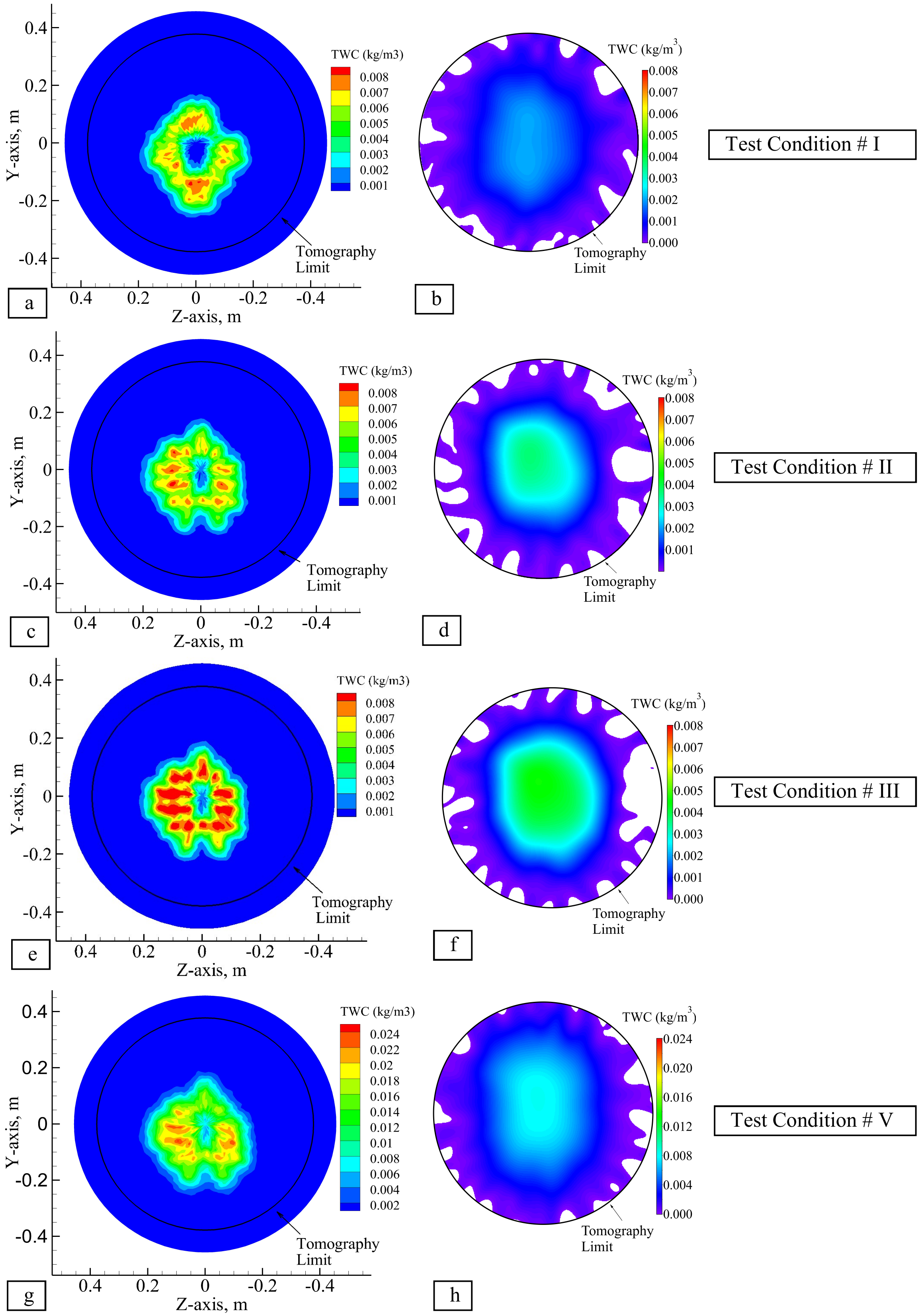

Figure 11: Comparison between simulation *TWC* predictions (a, c, e, and g) and experimental *TWC* data utilizing scaled tomography measurements (b, d, f, and h) for the four test conditions.

VI. Conclusion

Simulations of cloud development within the NASA Propulsion Systems Laboratory icing wind tunnel were performed utilizing the ANSYS Fluent Discrete Phase Model function. The purpose of these 3D simulations was to capture the thermodynamics and physics within the tunnel and to provide predictions of the test conditions at the test section of the tunnel (tunnel exit plane). Simulation predictions were compared with experimental data that were measured at the tunnel exit plane where initial cloud concentrations were not uniform across the tunnel inlet. The main focus in this paper was evaluating total water content, mass mixing ratio (humidity), and total air temperature between simulation and experiment. These are all of particular interest in icing research as it is crucial to accurately understand the conditions that lead to adverse icing. In many cases, multiple instruments were used for a particular measurement. Simulation predictions showed areas of agreement and disagreement.

The consistent variation against experimental data was that the simulated cloud, as it developed from the tunnel inlet spray nozzles, did not disperse as much as experimental data indicated. Simulations predicted that the cloud ejected from the spray nozzles follow the streamlines relatively closely for all considered conditions, creating water concentration profile shapes at the tunnel exit plane that correspond to the nozzle pattern used to create the cloud. For example, the nozzle configuration used to generate the cloud for all test conditions was “donut-shaped”, where no spray nozzles were activated in the center. Whereas there was some dispersion of the cloud, this generally resulted in low total water content concentrations at the center of the tunnel exit plane, and local high concentrations following streamlines from the nozzles at the inlet to the exit plane. Greater dispersion of the cloud from simulation could potentially match measured total water content more closely. A previous simulation study predicted that vortex shedding resulting from flow over the spray bar system created greater cloud dispersal [14]. In addition, this crosswise vortex shedding developed into streamwise vortices as flow developed through the contraction to the tunnel exit plane. This current paper did not model these additional complex geometries that would generate these large scale vortices, which may be the source for this disparity in cloud concentration.

This paper also evaluated the change in mass mixing ratio and the change in total air temperature due to cloud activation in the icing tunnel. During experiments, the humidity and air temperature changed in the presence of a cloud due to evaporation. The ANSYS simulations captured these evaporation effects both in magnitude and location reasonably well for most test conditions, when compared to test data. This result would suggest that the ANSYS simulation did not predict the spreading of the cloud as measured during experiment, but captured evaporation and the molecular movements of air and vapor relatively well. The simulations presented did not model droplet freezing, and as a result of not capturing the thermodynamics fully, likely provided a less accurate prediction of the thermal conditions. To highlight the importance of accurately knowing the conditions at the icing wind tunnel test section, total air temperature was measured and predicted to decrease by about 6 K when the cloud was activated for multiple test conditions. To understand the conditions that result in engine icing necessarily requires knowing the conditions that result during testing.

Appendix

Table A1: Details of the key parameters used to run the four simulations in ANSYS Fluent. Where a parameter varied between simulations, the value is listed in the order of Test Condition # I, II, III, and V, separated by semicolon.

General		
Solver	Pressure-Based	
Time	Steady	
Gravity	On (-9.81 m/s^2 in Y-direction)	
Operating Pressure (Pa)	44816	
Models		
Energy	On	
Viscous	Standard k-epsilon	
Species Transport	On	
Discrete Phase	On	
	Interaction with Continuous Phase	
	Droplet Coupled Heat-Mass Solution	
Injections	On	
	Total Injection Sites	19; 22; 22, 22
	Injection Type	Cone
	Number of Streams	30
	Particle Type	Droplet
	Material	Water-Liquid
	Diameter Distribution	Rosin-Rammler
	Evaporating Species	H_2O
	Cone Type	Solid Cone
	Uniform Massflow Distribution	On
	Injection Flow Direction	X-axis (positive)
	Temperature (^{O}C)	7.22
	Cone Angle (degrees)	45
	Outer Radius (m)	0.0016
	Minimum Diameter (m)	0.000003
	Maximum Diameter (m)	0.000195
	Mean Diameter (m)	0.000024
	Spread Diameter (m)	1.441615
	Number of Diameters	35
	Total Flow Rate – per nozzle (kg/s)	0.00287; 0.00358; 0.00515; 0.00896
	Drag Law	Spherical
	Turbulent Dispersions	Discrete Random Walk
Materials		
Air	Ideal Gas	
Water-Liquid	Droplet-Particle	
Aluminum	Solid	
Water-Vapor, Oxygen and Nitrogen	Fluid	
Boundary Conditions		
Mass Flow Inlet	Absolute Reference Frame	
	Mass Flow Rate (kg/s)	29.484; 45.133; 57.153; 45.133
	Flow Direction	X-axis (positive)
	Turbulent Intensity (%)	10
	Total Temperature (^{O}C)	7.22
	H_2O Species Mass Fraction	0.00483; 0.00469; 0.00469; 0.00498
	O_2 Species Mass Fraction	0.23
	Discrete Phase BC Type	Escape
Outflow	Discrete Phase BC Type	Escape
Walls	Wall Motion	Stationary
	Shear Conditions	No Slip
	Wall Roughness Model	Standard
	Thermal Condition	Heat Flux
	Heat Flux (W/m^2)	0 (adiabatic)
	Material	Aluminum
	Discrete Phase Boundary Condition Type	Reflect
Solution		
Pressure-Velocity Coupling Scheme	Coupled	
Residual Convergence Criteria	1E^{-2} for continuity, 1E^{-3} for the rest	

Acknowledgments

The authors wish to acknowledge the financial support for this work by the Advanced Aircraft Icing (AAI) sub-project of the NASA Advanced Air Transport Technology Project (AATT) under NASA's, Advanced Air Vehicle's program. In addition, the authors would also like to acknowledge Christopher Porter for his invaluable guidance in running CFD simulations, Timothy Bencic for providing tomography support, Thomas Ratvasky for analyzing Isokinetic Probe data, and Paul Von Hardenberg for his help in generating the probing location figure.

References

[1] Bravin, M., and Strapp, J.W., "A Continuiing Investigation of Diurnal and Location Trends in an Ice Crystal Icing Engine Event Data Base," *SAE International Conference on Icing of Aircraft, Engines, and Structures*, SAE, Minneapolis, MN, 2019, SAE Technical Paper 2019-01-1964.

[2] Mason, J. G., Strapp, J. W., and Chow, P., "The Ice Particle Threat to Engines in Flight," *44th AIAA Aerospace Sciences Meeting and Exhibit*, AIAA, Reno, NV, 2006, AIAA-2006-206.

[3] Flegel, A. B., "Ice Crystal Icing Investigation on a Honeywell Uncertified Research Engine in an Altitude Simulation Icing Facility," *Proceedings of the ASME Tubro Expo 2020*, London, England, 2020, GT2020-14714.

[4] Flegel, A. B., and Oliver, M. J., "Preliminary Results from a Heavily Instrumented Engine Ice Crystal Icing Test in a Ground Based Altitude Test Facility," *8th AIAA Atmospheric and Space Environments Conference*, 2016, AIAA-2016-3894.

[5] Oliver, M. J., "Validation Ice Crystal Icing Engine Test in the Propulsion Systems Laboratory at NASA Glenn Research Center," *6th AIAA Atmospheric and Space Environments Conference*, AIAA, Atlanta, GA, 2014, AIAA-2014-2898.

[6] Struk, P. M., Agui, J. H., Bartkus, T. P., Tsao, J.-C., King, M. J., and Ratvasky, T. "Ice-Crystal Icing Accretion Studies at the NASA Propulsion Systems Laboratory," *SAE 2019 International Conference on Icing of Aircraft, Engines, and Structures*, SAE, Minneapolis, MN, 2019, SAE Technical Paper, 2019-01-1921.

[7] Bartkus, T. P., Tsao, J. C., and Struk, P. M. "Analysis of Experimental Ice Accretion Data and Assessment of a Thermodynamic Model During Ice Crystal Icing " *SAE International Conference on Icing of Aircraft, Engines, and Structures*, SAE Technical Paper, 2019-01-2016.

[8] Struk, P. M., Ratvasky, T. P., Bencic, T., Van Zante, J. F., King, M. C., Tsao, J.-C., and Bartkus, T. P. "An Initial Study of the Fundamentals of Ice Crystal Icing Physics in the NASA Propulsion Systems Laboratory," *9th AIAA Atmospheric and Space Environments Conference*, AIAA, Denver, CO, 2017, AIAA-2017-4242.

[9] Struk, P. M., Tsao, J-C., and Bartkus, T. B., "Plans and Preliminary Results of Fundamental Studies of Ice Crystal Icing Physics in the NASA Propulsion Systems Laboratory," *8th AIAA Atmospheric and Space Environments Conference*, 2016, AIAA-2016-3738.

[10] Van Zante, J. F., Ratvasky, T. P., Bencic, T. J. Challis, C. C., et al. " Update on the NASA Glenn Propulsion Systems Lab Icing and Ice Crystal Cloud Characterization (2017)," *2018 AIAA Atmospheric and Space Environments Conference*, AIAA, Atlanta, GA, 2018, AIAA-2018-3969.

[11] Van Zante, J. F., Bencic, T. J., and Ratvasky, T. P., "Update on the NASA Glenn Propulsion Systems Lab Ice Cloud Characterization Update 2015," *8th AIAA Atmospheric and Space Environments Conference*, AIAA, Washington D.C., 2016, AIAA-2016-3897.

[12] Van Zante, J. F., and Rosine, B. M., "NASA Glenn Propulsion Systems Lab: 2012 Inaugural Ice Crystal Cloud Calibration," *6th AIAA Atmospheric and Space Environments Conference*, AIAA, Atlanta, GA, 2014, AIAA-2014-2897.

[13] Griffin, T. A., Dicki, D. J., and Lizanich, P. J., "PSL Icing Facility Upgrade Overview," *6th AIAA Atmospheric and Space Environments Conference*, AIAA, Atlanta, GA, 2014, AIAA-2014-2896.

[14] Feier, I., "Numerical Investigation of the NASA Glenn Propulsion Systems Laboratory," *SAE 2019 International Conference on Icing of Aircraft, Engines, and Structures*, SAE, Minneapolis, MN, 2019, SAE Technical Paper, 2019-01-1924.

[15] Struk, P. M., King, M. C., Bartkus, T. P., Tsao, J-C., Fuleki, D., Neuteboom, M., and Chalmers, J. L., "Ice Crystal Icing Physics Study Using a NACA 0012 Airfoil at the National Research Council of Canada's Research Altitude Test Facility," *2018 AIAA Atmospheric and Space Environments Conference*, AIAA, Atlanta, GA, 2018, AIAA-2018-4224.

[16] Struk, P. M., Tsao, J., and Bartkus, T., "Plans and Preliminary Results of Fundamental Studies of Ice Crystal Icing Physics in the NASA Propulsion Systems Laboratory," 8th AIAA Atmospheric and Space Environments Conference, AIAA, Washington D.C., 2016, AIAA 2016-3738.

[17] Struk, P., Bartkus, T., Tsao, J., Currie, T., and Fuleki, D., “Ice Accretion Measurements on an Airfoil and Wedge in Mixed-Phase Conditions,” *SAE 2015 International Conference on Icing of Aircraft, Engines, and Structures*, SAE, Prague, Czech Republic, 2015, SAE Technical Paper 2015-01-2116.
[18] Struk, P. M., Bencic, T., Tsao, J., Fuleki, D, and Knezevici, D. C. “Preparation for Scaling Studies of Ice-Crystal Icing at the NRC Research Altitude Test Facility,” 5th AIAA Atmospheric and Space Environments Conference, AIAA, San Diego, 2013, AIAA-2013-2675.
[19] Bartkus, T. P., Struk, P. M., and Tsao, J.-C., "Comparisons of Mixed-Phase Icing Cloud Simulations with Experiments Conducted at the NASA Propulsion Systems Laboratory," *9th AIAA Atmospheric and Space Environments Conference*, 2017, AIAA-2017-4243.
[20] Bartkus, T. P., Struk, P. M., Tsao, J. C., and Van Zante, J. F., "Numerical Analysis of Mixed-Phase Icing Cloud Simulations in the NASA Propulsion Systems Laboratory," *8th AIAA Atmospheric and Space Environments Conference*, 2016, AIAA-2016-3739.
[21] Bartkus, T. P., Struk, P. M., and Tsao, J. C., "Development of a Coupled Air and Particle Thermal Model for Engine Icing Test Facilities," *SAE Int. J. Aerosp.* Vol. 8, No. 1, 2015. p. 15-32, doi: 10.4271/2015-01-2155.
[22] Agui, J. H., Struk, P. M., and Bartkus, T. P. "Total Temperature Measurements in Icing Cloud Flows using a Rearward Facing Probe," *SAE International Conference on Icing of Aircraft, Engines, and Structures*, SAE, Minneapolis, MN, 2019, SAE Technical Paper 2019-01-1923.
[23] Agui, J. H., Struk, P. M., and Bartkus, T. P. "Total Temperature Measurements Using a Rearward Facing Probe in Supercoooled Liquid Droplet and Ice Crystal Clouds,” *2018 AIAA Atmospheric and Space Environments Conference*, AIAA, Atlanta, GA, 2018, AIAA-2018-3970.
[24] Agui, J. H., Struk, P. M., Chen, R. C., Bartkus, T. P., and von Hardenberg, P. "Cloud Uniformity Measurement from NASA's 2nd Fundamental Ice Crystal Icing Test - Part 2 (Temperature & Humidity)," *11th AIAA Atmospheric and Space Environments Conference*, AIAA, Reno, NV, 2020 (submitted for publication).
[25] Chen, R. C., Struk, P. M., Ratvasky, T. P., and Agui, J. H. "Cloud Uniformity Measurement from NASA's 2nd Fundamental Ice Crystal Icing Test - Part 1 (Water Content & PSD)," *11th AIAA Atmospheric and Space Environments Conference*, AIAA, Reno, NV, 2020 (submitted for publication).
[26] Lilie, L., Emery, E., Strapp, J. W., and Emery, J. "A Multiwire Hot-Wire Device for Measurement of Icing Severity, Total Water Content, Liquid Water Content, and Droplet Diameter,” *43rd AIAA Aerospace Sciences Meeting and Exhibit*, AIAA, Reno, NV, 2005, AIAA-2005-859.
[27] Lilie, L. E., Sivo, C. P., and Bouley, D. B., “Description and Results for a Simple Ice Crystal Detection System for Airborne Applications,” *8th AIAA Atmospheric and Space Environments Conference*, 2016, AIAA-2016-4058.
[28] Strapp, J. W., Lilie, L. E., Ratvasky, T. P., Davison, C. R., and Dumont, C., “Isokinetic TWC Evaporator Probe: Development of the IKP2 and Performance Testing for the HAIC-HIWC Darwin 2014 and Cayenne Field Campaigns," *8th AIAA Atmospheric and Space Environments Conference*, AIAA, Washington D.C., 2016, AIAA-2016-4059.
[29] King, M. C., Manin, J., Van Zante, J. F., Timko, E. N., and Struk, P. M., "Particle Size Calibration in the NASA Propulsion Systems Laboratory," *2018 AIAA Atmospheric and Space Environments Conference*, AIAA, Atlanta, GA, 2018, AIAA-2018-3971.
[30] Stickney, T.M., Shellow, M.W., and Thomspon, D.I. "Goodrich Total Temperature Sensors," 1994, Goodrich Technical Report 5755.
[31] Bencic, T., Fagan, A., Van Zante, J. F., Kirkegaard, J. P., Rohler, D. P., Maniyedath, A., and Izen, S. H., "Advanced Optical Diagnostics for Ice Crystal Cloud Measurements in the NASA Glenn Propulsion Systems Laboratory," *5th AIAA Atmospheric and Space Environments Conference*, AIAA, San Diego, CA, 2013, AIAA-2013-2678.